Titanium-dioxide nanostructures grown by dual DC/HiPIMS for dye-sensitized solar cell applications

K. Grigorov[a,c], J. Libardi[b], R. Moraes[d], A.S. da Silva Sobrinho[b], M. S. Oliveira[e], D.M.G. Leite[b], M. Massi[c]* ⓘD

[a]Bulgarian Academy of Sciences, Space Research and Technology Institute, Acad. G. Bonchev Str. Bl.1, 1113, Sofia, Bulgaria.
[b]Instituto Tecnológico de Aeronáutica (ITA), Laboratório de Plasmas e Processos (LPP), São José dos Campos, SP, Brasil.
[c]Universidade Presbiteriana Mackenzie, Escola de Engenharia (PPGEMN), São Paulo, SP, Brasil.
[d]ETEC Prof. Ilza Nascimento Pintus, São José dos Campos, SP, Brasil,
[e]Universidade Federal de São Paulo, Instituto de Ciência e Tecnologia, São Paulo, SP, Brasil.

This work reports how the solar conversion efficiency of dye-sensitized solar cells (DSSCs) depends on the crystalline structure of both the compact TiO_2 blocking layer (BL) and homoepitaxially grown porous TiO_2 mesoporous structure. The films were grown by simultaneous sputtering of titanium targets by DC magnetron and by high-power impulse magnetron systems (HiPIMS). The deposition conditions were managed to produce *in situ* dense BLs and porous TiO_2 films. The only variable was the polarization of the BLs (0 to -200V). The polarization caused phase transformations from pure anatase phase through rutile-anatase mixed phases to rutile phase. The polarization results in decreasing intensity of the anatase (101) peak of the porous layers. The latter promptly decreased linearly the value of the short-current Isc and exponentially the open-circuit voltage Voc of the cells. Another inference is the surface energy of the BLs, which follows an exponential decay as a function of the film polarization. XPS study of the Ti $2p_{3/2}$ – Ti $2p_{1/2}$ doublet reveals an appearance of a shake-up satellite, whose area exponentially decreases as the polarization potential rises. This phenomenon is discussed and related with other physical aspects of the homo-epitaxially grown films with different texture. The anatase phase content and its purity predefined by the experimental conditions determine the quality of the DSSC, as well as other components such as the dye type, the electrolyte, and the electrode materials.

Keywords: *DSSC, Titanium dioxide, Blocking Layer, HiPIMS, Solar Cell Efficiency, XPS, Surface Energy.*

1. Introduction:

Many researchers have spent considerable efforts optimizing the dye-sensitized solar cells (DSSCs) since their discovery[1]. Naturally, these efforts have been divided between the many elements of the cells, such as the photo-anode material and its structure[2-4], the nature of the dye (inorganic or organic), and the transparent conducting oxide (TCO) type placed on both the photo-anode and the counter electrode side[5,6]. The use of Blocking Layers (BLs) creates another important branch of studies, as their use in the most cases enhances the performance of the DSSCs[7-10]. The purposes of the BL are to guarantee a smooth and defect-free hetero- or homo-epitaxial growth of the next film and to prevent current leakage[7] when electrolyte with redox couple, or electron-hole recombination (HTM) are used. Various BLs deposited by RF sputtering, such as TiO_2, Nb_2O_5, and ZnO were investigated for possible application in DSSCs. The conversion efficiency (η) and the short circuit current (Jsc) values of the DSSC using Nb_2O_5 as blocking layer achieve the best improvement of 26.9% and 35.5%, respectively[11].

Many researchers have studied how the nature, chemistry, crystallinity, thickness, and phase purity of BLs influence the device performance. Sung[12] related that inserting BL between the FTO and the nano-porous TiO_2 layer lead to 37% increased shunt resistance (R_{SH}) when the BL thickness is greater than 60 nm and also established the optimum BL thickness. Defect free and dense blocking layer structure prevents electrolyte shortening and electron leakage maintaining high cells shunt resistance. In addition, the porosity of the sintered nanocrystal material, such as TiO_2, ZnO, and Al_2O_3, plays a central role in the solar cell architecture, if electrolyte-based DSSC, ssDSSC, or perovskite mesoporous scaffold structures are used[13]. Optimising the mesoporous TiO_2 structure enhances the connectivity and diffusion through the mesoporous network as well as the light harvesting[13,14].

Different deposition techniques aim to produce a compact TiO_2 on the anode side and a porous nanocrystalline TiO_2 acting as a skeleton semiconductor material where the dye molecules would be fixed and a sufficient electrolyte absorbed. Physical, morphological, and chemical peculiarities arise from the use of different deposition techniques. In addition to Magnetron Sputtering (MS) methods, spin coating or spray pyrolysis and, recently, atomic layer deposition (ALD) are methods that yield pin-hole-free and dense structure suitable

for the purposes cited above. The BL influences the cell performance through the quality of the mesoporous layers and, in general, determines their resistivity[15]. To increase the cell performance, particularly its conductivity, some authors[16] have used graphene nano-flakes, which provide good charge-collection.

From the physical vapour deposition (PVD) techniques, a promising method is High-power Impulse Magnetron Sputtering (HiPIMS), which is known as a versatile and powerful tool for depositing thin film . Among the many papers concerning HiPIMS, the work of Greczynski et al.[17] describes a hybrid HiPIMS/magnetron co-sputtering configuration used to achieve high hardness and low residual stress of $Ti_{1-x}Al_xN$ alloys. The transport processes occurring in HiPIMS was studied in detail in Straňák[18] work.

Even though the use of BL has been the focus of many studies, researchers have not unconditionally proven how and to what extent the structure of the BL influences the cell energy conversion capability. The BL is expected to have a densely packed crystalline structure to prevent the electrolyte from contacting the anode. As we shall see later, the mentioned condition is far from sufficient. To assure a different degree of film density, a negative polarization up to 200 V was applied during BL film growth. In addition to the XRD analyses, the XPS spectra were considered and the effect of the plasmon-like shake-up satellite of Ti $2p_{3/2}$ was studied in respect the BL polarization. Furthermore, it was shown how the BL film texture and phase composition influence the quality of the nano-porous films, affecting the electrical behaviours of the cell. Correlations between the surface energy (SE) of the BLs and their phase content have been discussed. A noticeable one-to-one dependence of the short circuit current (I_{SC}) and the open voltage (V_{OC}) on the Anatase peak (101) intensity from the next grown porous films were also shown and discussed.

2. Experimental details

BLs films were deposited by both dual DC and HiPIMS magnetron systems onto (100) c-Si and FTO/glass substrates. Then, without breaking the vacuum in the system, porous TiO_2 films were deposited onto the BLs, using the same power supplies. The samples were assembled with the counter-electrode made from transparent Pt/FTO/glass, to construct solar cells.

The choice of two magnetrons performing together comes from the relatively low deposition rate (depending on the power and pulse t_{on}) characteristic for HiPIMS. Both magnetrons/ targets were placed in plane at an angle of 45 degrees facing the substrate at distance of 12 cm.

The BL deposition was conducted for 90 min (plus 20 min pre-sputtering) in argon and oxygen flow of 7.3 and 7.34 sccm,

respectively, yielding a working pressure of 2.55 mTorr. The HiPIMS experimental parameters were power – 180 W; frequency – 400 Hz; and pulse t_{on} – 60 µs (duty cycle – 2.4%). The DC magnetron was powered by 150 W. The only variable was the polarization of the substrate ranging from 0 to -200 V.

Further, the BLs were denoted as S1, S2, S3, and S4 corresponding to 0 V, -50 V, -100 V, and -200 V bias, the porous TiO_2 deposited *in situ* onto the BLs were denoted as M1, M2, M3, and M4 for those with average thickness of 225 nm, and as M1*, M2*, M3*, and M4* with average thickness of 170 nm. Those abbreviations are listed in Table 1.

The nano-porous TiO_2 films were deposited by adding a small amount of N_2 to the gas mixture (0.9 sccm). Grigorov et al.[19] and Nakamura et al.[20] studied the effect of N_2-content on the narrowing of the TiO_2 bandgap, which rendered it more transparent, consequently rising the cell efficiency. The argon and the oxygen flows were kept similar to the BL depositions. However, the HiPIMS power was maintained at 140 W and the DC magnetron power at 250 W. Two batches were deposited for 105 and 180 min, yielding thickness of 170 nm (4 samples) and 225 nm (4 samples), respectively. The working pressure was kept at 2.6 mTorr, argon at 1.21 mTorr, oxygen at 1.24 mTorr, and nitrogen at 0.15 mTorr. The exact film thicknesses were calculated by ellipsometry and reflectometry (XRR).

The porous TiO_2 films were sensitized using Ruthenium N-3 complex, in which 12 mg of the N3-dye were diluted to 60 mL of ethanol (99.5%). Then the already prepared samples (glass/FTO/BL/porous TiO_2) were immersed for 24 hours in room temperature. By the end of the dye absorption process, the samples differed in colour saturation according to the degree of its porosities. The electrolyte used in this study was the ionic redox Iodolyte HI-30® (purchased from Solaronix™) based on Iodide/Triiodide Redox couple I^-/I_3^{-}[21] with concentration 30 mM in acetonitrile with additives - ionic liquid, lithium salt, pyridine derivative, thiocyanate[22]. The role of the electrolyte is to regenerate oxidized ruthenizer® (purchased from Solaronix™).

The films were characterized by Scanning Electron Microscopy with Field Effect Gun (SEM-FEG), X-ray diffraction (XRD) measurements, atomic-force-microscope (AFM), Contact Angle, and X-ray photoelectron spectrometry (XPS). The morphology of the BLs and the porous TiO_2 films was studied using a Shimadzu SPM-9500 J3 atomic force microscope (AFM). The phase composition of the BLs was characterized by Grazing Incidence X-ray diffraction (GIXRD) with PANalytical Empyrean system equipped with a multichannel detector (Pixel 3D) using (Cu $K\alpha$ 45 kV-40 mA) radiation. The energy-conversions efficiency of the solar cells was measured by means of ($\sim$100 mW/cm²) AM 1.5 solar simulators.

Table 1. Polarization values and associated abbreviations adopted for the BLs and the porous TiO_2 films used in Figures 5 to 10 and Tables 2 to 4.

Cell #	1	2	3	4	5	6	7	8
Bias [V]	0	-50	-100	-200	0	-50	-100	-200
BL	S1	S2	S3	S4	S1	S2	S3	S4
Porous I	M1	M2	M3	M4				
Porous II					M1*	M2*	M3*	M4*

3. Results and Discussions

3.1. Morphological and structural peculiarities

In Figure 1, a SEM micrograph of BL deposited at bias of -50 V is shown at a magnifcation of 20 kX. The sample has a flat surface, as later confirmed by AFM, and the charging effect made it difficult to obtain sharp images for most samples. They were composed with a dense mixture of rutile-anatase phases. Similar results for a BL, called compact layer, was reported by the group of Chang et al.[23]. Some structural and physico-chemical parameters of the BLs are calculated and summarized in Table 2. The porous titanium dioxide presented different structure than the BLs, Figure 2a and 2b, composed of well-defined randomly oriented grains with dimensions between 200 and 400 nm. In accordance with the data obtained by SEM and AFM, at least 25% of porosity was achieved. The porosity depends strongly on the film phase composition and allows them to efficiently absorb
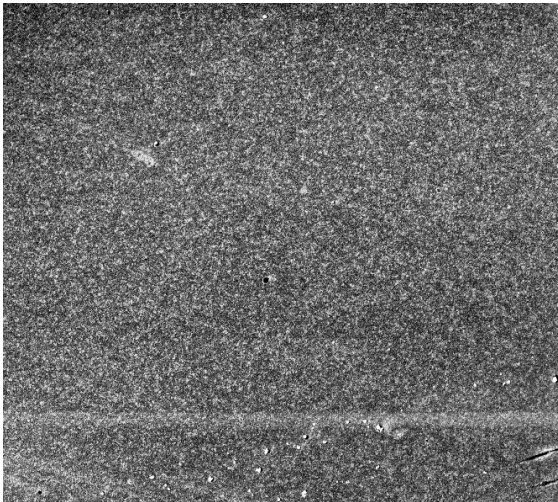
the dye on their internal surface. The overall film thickness is important for the final cell performance. Its maximum thickness should vary depending on film transparency or the light absorption coefficient of the structure.

The AFM scans were acquired in dynamic mode and areas of 3×3 μm and 1×1 μm were selected. Figure 3 presents a scan of porous TiO_2 deposited onto intact BL (0 V), together with its grain-size distribution. The RMS roughness is 37.3 nm.

According to the SEM images in Figure 2b, the TiO_2 microcrystals are grouped in well-distinguished grains with 250 nm mean diameter randomly distributed in the volume, which guarantees good degree of porosity. The grains could be roughly approximated to a sphere shape, and even if the greatest fraction of space occupied by spheres is $\pi/(3\sqrt{2}) \cong 0.74$ in hcp lattice, the calculations based on four adjacent spheres indicate that 28% of its volume is due to pores. In Figure 3 and Figure 4, the AFM scans of porous TiO_2 onto BL(0) and compact only BL(-50 V) confirm the huge difference of their morphology. The mean grain radius was 110 nm and 10.5 nm for the porous and the compact layers, respectively. Both scans were taken at different scaling factors, and if equated, the differences in their morphology appears strongest. Keep in mind that in sense of porosity or "active" surface onto, which the dye sensitizing molecules accommodate, the sphere shape surface increases with the square of its radius, leading to 120 time greater surface for sphere with radius 110 nm than 10.5 nm.

The BL (-50 V), shown in Figure 4, has 12.8 nm RMS roughness and uniform grain radius distribution. On the other hand, the AFM images of the BLs deposited by higher bias are distinguished by their very flat surfaces with roughness below 2 nm, and they could be considered as compact with porosity below 5%.

The X-ray diffraction patterns for the as-deposited blocking layers with substrate polarization - 0 V, -50 V, and -100 V, called hereafter as S1, S2, and S3 are shown in Figure 5. The porous TiO_2 films, deposited subsequently *in situ* onto the BLs are denotes as M1, M2, M3, and M4 with 275 nm
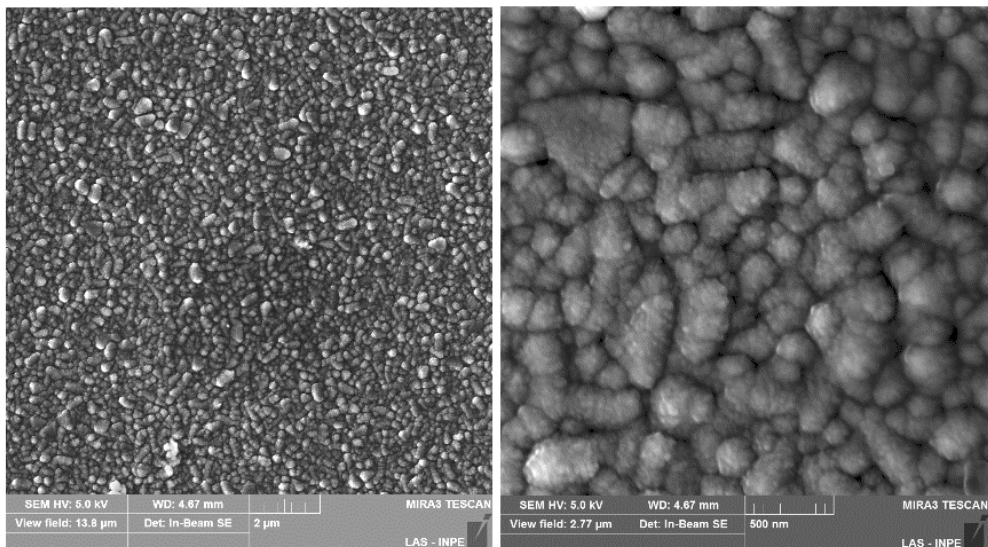

Figure 1. SEM micrographs (20kX) of fine-grain structure BL (-50 V).

Figure 2. SEM micrographs of 225 nm thick porous TiO_2 layer deposited onto BL(0V) at different magnificent - a) at 20 kX and b) 100 kX.

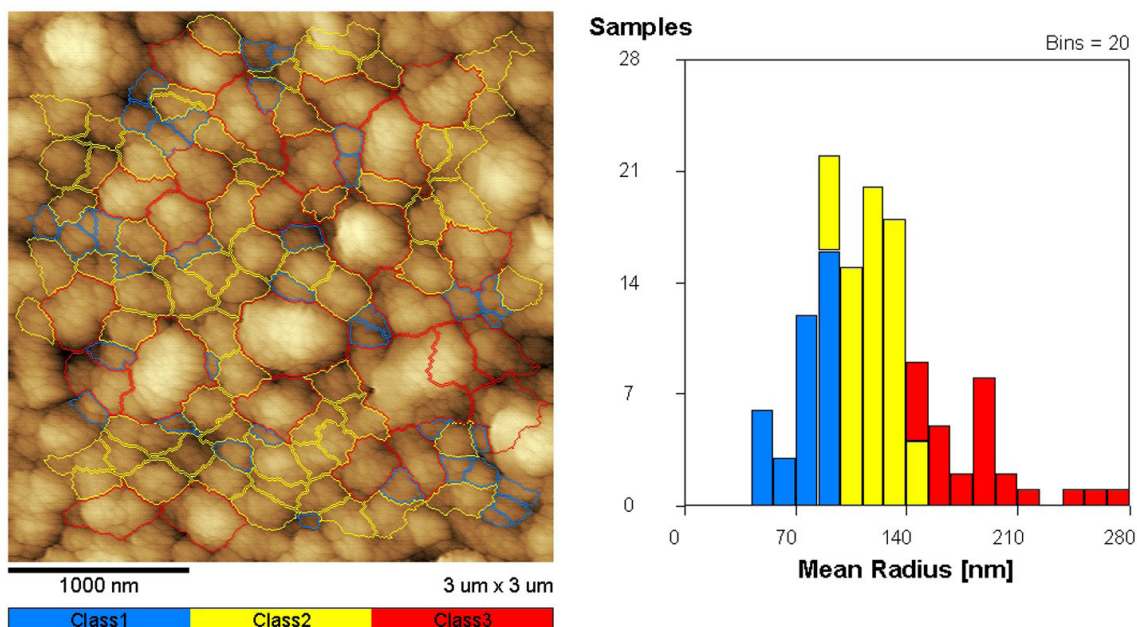**Figure 3.** AFM on (3 × 3) μm scan of the porous TiO_2 deposited onto BL (0 V) and the mean grain radius distribution.

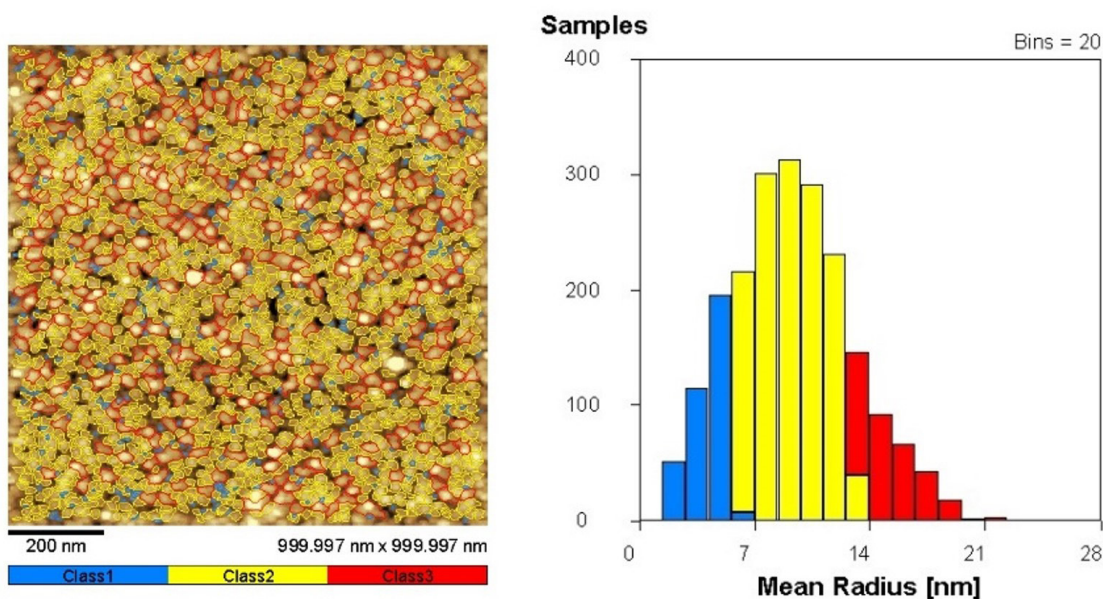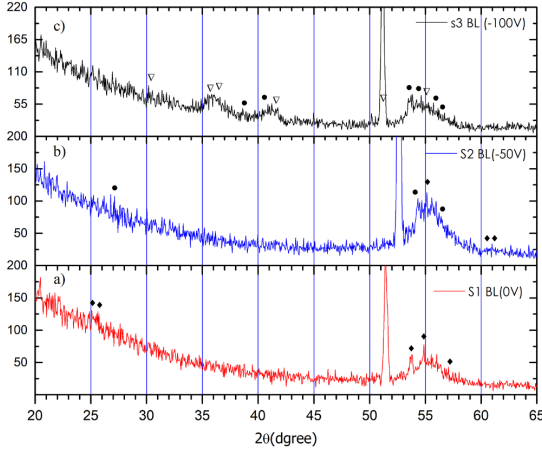**Figure 4.** AFM on (1 × 1) μm scan of the BL (-50 V) and the mean grain radius distribution.

thickness and with M1*, M2*, M3*, and M4* with 175 nm thickness (Table 1).

All BL thicknesses were about 100 nm. Such thicknesses did not favor a strong signal reflected from the atom's plans. Moreover, lattice mismatch between the FTO and the BL formed a disordered interface layer, whose thickness depended on the deposition conditions and the substrate quality. The strong reflection above 50° 2θ presented in the spectra was due to the total internal reflection (TIR) from a thin film laying on a flat surface. This phenomenon, which occurs at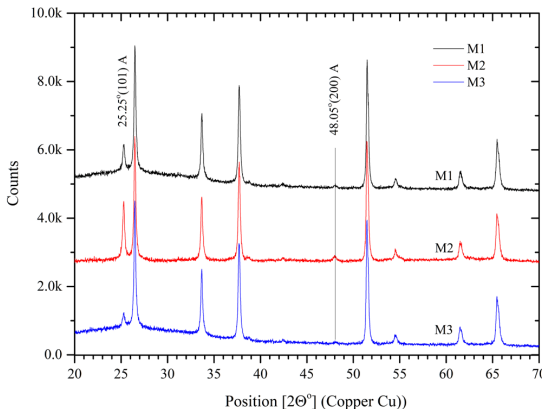 a specific critical angle of incidence is confirmed by the lack of reflections at angles of incidence greater than 0.25°. TIR is observed for all the spectra shown in Figure 5, but they are not aligned with each other, as the latter depends on small variations in the thickness of the layers.

The XRD spectrum of BL (S1) deposited at zero bias is presented in Figure 5a. It was composed only by Anatase phases, pdf numbers; 86-1157; 89-4203; and 71-1169, with 38%, 60%, and 2% content, respectively (Table 2). These compositions yield a mean density of $\rho = 2.48$ g/cm^3, mean cell volume of $V = 136.5$ Å^3, and an average atomic mass of $N_A = 4.48.10^{14}$ at/cm^2/Å.

Applying a bias, Figure 5b and 5c, caused partial to almost total phase transformations from Anatase to the high temperature Rutile phase. The BL deposited at -50 V bias, in Figure 5b, was constituted of Anatase phases; 04-0477 and 71-1169 with phase concentrations 55% and 35%, respectively, and a Rutile phase 77-0446 – 10%, in which $\rho = 3.89$ g/cm^3, V = 113 Å^3, and the average atomic mass was $N_A = 7.10^{14}$ at/cm^2/Å. In Figure 5c, BL deposited at -100 V bias is shown, which consisted of Rutile phases pdf numbers (76-0321; 88-1174) – 34%, and titanium oxide tetragonal phase 84-1750. Consequently, its density reached $\rho = 4.31$ g/cm^3, the mean volume of cell drops of V = 82 Å^3, and the atomic density – $7.8.10^{14}$ at/cm^2/Å. The Anatase phases disappeared or were transformed. The applied substrate polarization led to an increased density of the ion flux toward the growing film, increasing its temperature and ad-atom mobility[24-26]. Table 2 summarizes these results.

XRD spectrum of the porous TiO$_2$ (M1, M2 and M3) deposited onto BL (0V) are presented in Figure 6 and refers to one of the highest qualities of Anatase structures with 25.27° and 48.03° reflection planes (101) and (200), respectively. Other peaks are due to the crystalline TCO – the fluorine tin oxide (FTO). The reflection (200) is shifted slightly to higher 2θ degree (0.01°), suggesting cell distortion. The latter is due to of the incorporation of N$_2$ (~5%) as interstitials. N$_2$ decreases the value of the semiconductor bandgap[19,20]. Based on Bragg's law and bearing in mind the Cu anode in use, the cell parameter increased with 0.01 Å for plane (101) and decreased with 0.003 Å for plane (200). This increase in the volume affected the electronic structure in a complex manner by reducing the band gap of TiO$_2$ and raising the electron velocities. Nakamura et al.[20] explained that the N-doping results in a mid-band gap energy level, which reduces the energy of the entire transition process.

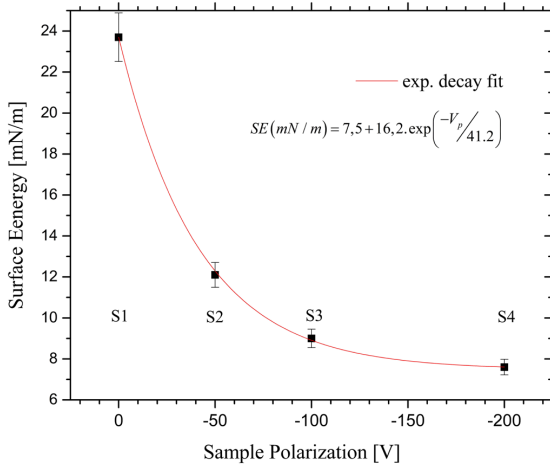## 3.2. Film chemistry and phase composition

As previously described, Table 2 contains data about the BL phase composition, density, cell volume, atomic density, surface energy, energy of adhesion, and the ion-dose received during the film growth. Table 2 refers only to BLs as they define the quality of the next growth layer – the porous TiO$_2$. Only as a reference, the porous M1 grown onto S1 BL exhibited values for the surface energy SE = 25.2 mN/m^2 and energy of adhesion W_A = 137.2 mJ/m^2, values close to those of BL S1. The unbiased BL (S1) was build up by anatase only phases with higher cell volume yielded porous film with lower density. The decrease of the surface energy, shown in Figure 7, obviously affects the adherence of the adjacent films (M1…M4) leading to a poor crystallographic orientation and vanishing the reflections from plane (101) at 25.27° 2θ (Figure 6). This behaviour was successfully

Figure 5. GIXRD spectra of blocking layers deposited with a) 0 V b) -50 V, c) -100 V bias. ♦ -Anatase phase; • - Rutile phase; and ∇ - titanium oxide tetragonal phase.

Figure 6. XRD spectra of porous TiO$_2$ films deposited onto BL (0V – M1; -50 V – M2; -100 V – M3)/FTO/Glass. Anatase only content - Ref. Pattern pdf N° 071-1169.

Table 2. Blocking layers; A- Anatase; R -Rutile; T-tetragonal, the average mass density, volume cell, atomic mass, surface energies (polar components), work of adhesion (W_A), and the ion bombardment flux.

BL	Bias [V]	Phases Pdf N^0	%	ρ [g/cm^3]	V [Å^3]	N_A [at/cm^2/Å]	SE [mN/m]	W_A [mJ/m^2]	I_d [10^{17}ion/cm^2.s]
S1	0	86-1157 (A)	38	2.48	136.5	4.48	23.7	130.2	0.85
		89-4203 (A)	60						
		71-1169 (A)	2						
S2	-50	04-0477 (A)	55	3.89	113	7.0	12.1	110.5	1.4
		71-1169 (A)	35						
		77-0446 (R)	10						
S3	-100	76-0321(R)	20	4.31	82	7.8	8.8	101.2	3.0
		84-1750 (T)	65.7						
		88-1174 (R)	14.3						

correlated with the cell I(V) characteristics – I_{SC} and V_{OC} and shown in Figure 8 and Figure 9, respectively.

The Binding Energy (BE) of Ti 2p was considered for all BLs, where the doublet Ti $2p_{3/2}$ – Ti $2p_{1/2}$ migrated to

lower energies ranging from 457.9 eV to 456.7 eV for S1 to S4, respectively, due to Ti^{4+} reduction, but the spin-orbital splitting remained constant ($\Delta = 5.69$ V). Interesting behaviour is followed by the shake-up satellite of Ti $2p_{3/2}$, precisely its surface evolution as a function of the film polarization. These results are illustrated in Figure 10. When a perfect Anatase crystal is excited by *hv*, a photoelectron from K-shell is ejected through the Fermi level to the Vacuum, meanwhile an electron from one of the four O atoms is drawn to substitute the photoelectron, leaving one O$^+$. This process ends up such as the Plasmon losses in metals where collective vibration of the free electron gas is registered. Even negligible, the positive generated charge (O$^+$) slows down the priory emitted photo e$^-$. As the XPS detector measures kinetics energies and *hv* is a constant parameter, the resulting Binding Energy (BE) is higher, which is why the shake-up satellites appear at higher BE than the characteristic Ti $2p_{3/2}$ or Ti $2p_{1/2}$. By itself, the shake-up satellite surface decrement means reduced Ti^{4+} states, descending into lower homological states than TiO$_2$. The latter is also proved by the shift of the doublet Ti $2p_{3/2}$ – Ti $2p_{1/2}$, which migrates to lower binding energies. The similarity of both derived exponential decay constants (Figure 7 and Figure 10) (t)

$$SE(mN/m) = 7,5 + 16,2 . \exp\left(\frac{-V_p}{41.2}\right)$$

Figure 7. Surface energy dependence on the BL polarization.

$$I_{SC} = 0.52 + 0.000477 \; PI$$
$$R^2 = 0.996; \; \sigma = 0.017$$
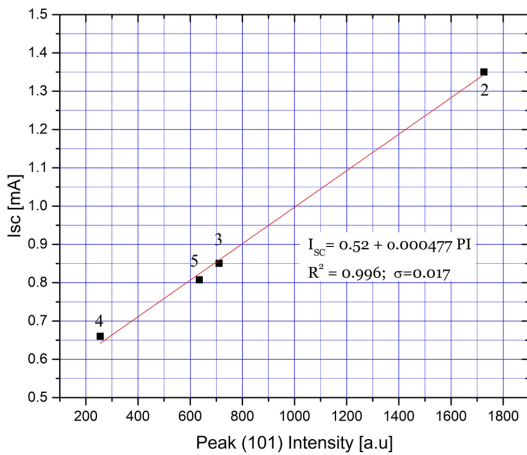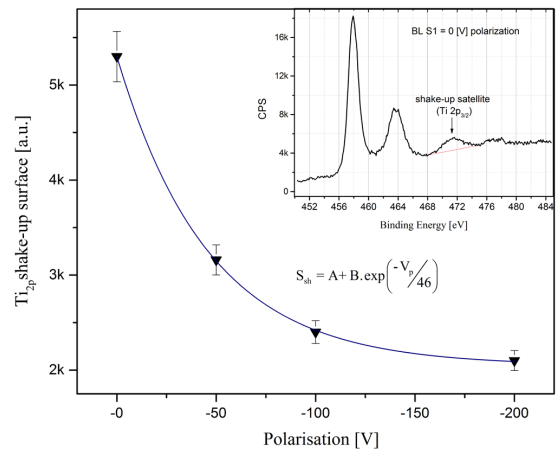
Figure 8. Correlation between the cell short current I_{SC} and the Anatase (101) peak intensity.

$$V_{oc} = 0.72 - 2.45 e^{-PI/166}$$
$$R^2 = 0.999; \; \sigma = 0.008$$
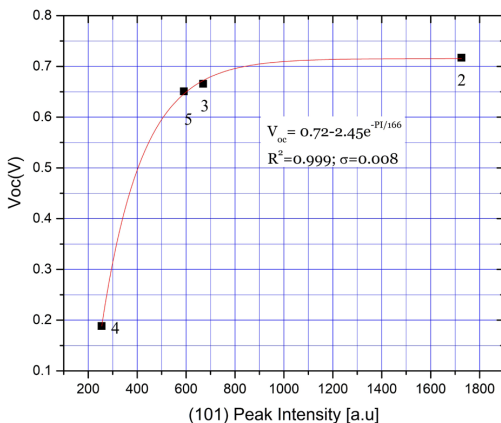
Figure 9. Open-circuit voltage V_{OC} dependence on the Anatase (101) peak intensity.

$$S_{sh} = A + B . \exp\left(\frac{-V_p}{46}\right)$$

Figure 10. Ti 2p3/2 shake-up satellite surface dependence on BL polarization. Inset; TiO$_2$ XPS spectrum of S1 (VP = 0V).
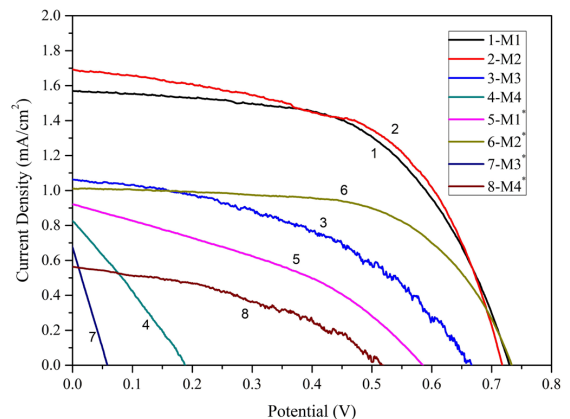
Figure 11. Current-voltage plot of the studied DSSCs.

$\cong 40$ V demonstrates a common origin of the discussed phenomena. This value suggests that ion flux in the range of $0.8.10^{17}$ to $1.4.10^{17}$ at/cm²/s contributed to the formation of the optimal crystalline structure and surface energy with respect to the already discussed context. Ion bombardment exceeding this limit results in reduction of Ti^{4+} states and oxygen deficiency followed by generations of sub-oxides.

The resulting BL films, even denser, have poor quality from the chemical standpoint, as defect induced impurities act as traps to split the valence band of the semiconductor. Thus, the adhesion of the adjacent layers was poor and did not promote oriented crystal growth of the consequent functional layer. The I(V) characteristics, shown in Figure 11 clearly depict the consequences of the different crystalline structure and the different valence states of TiO_2 on their characteristics. First, the increase of the serial resistance Rs of the cell led to falling slope at Voc and was related with the porosity volume and the quantity of chemisorbed dye on its surface, whereas decreasing the shunt resistance R_{SH} states created bad semiconductor or bad compact layers - shortening the cell structure. Table 3 summarizes data on the I(V) curve shunt, serial resistance of samples 3 and 6, their peak (101) intensity, and FWHM. Both curves are characterized by similar J_{SC} values, but have different FF and output power (Figure 11).

Sample 6 has almost infinite shunt resistance, which is much lower in sample 3. This unequivocally affirms in sample 3 the flaws, such as structural defects, mismatches, and higher metallic content than a perfect semiconductor (Anatase in the case). Sample 3 contains BL polarized with bias voltage – 100 V, whereas sample 6 – with -50 V. During the magnetron deposition, negative bias accelerates positive ions extracted from the plasma together with some heavy radicals. Instead of causing structure densification of the growing films, they lead to its destruction up to different degree. The serial resistance of both samples was estimated, and the summarized results are shown in the Table 3. The R_S of sample 3 is almost double that of sample 6, which suggests decreased porosity and bad interconnections (crystalline alignments) impeding the charge flow. The latter obviously affects the quantity of the adsorbed dye. Even though sample 3 represent a bit better peak intensity (Table 3) (coming from the thicker porous film 225 vs 170 nm), its FWHM value is greater than that of sample 6, suggesting better structure alignment and all the consequences arising from that.

3.3. Peculiarities of the studied PV Solar Cells

In general, the open-circuit voltage (V_{OC}) corresponds to the inherent voltage of the cell generated by the sun light causing a flow of photoelectrons, whereas the short current (I_{SC}) describes the maximum drained current when the voltage applied by the potentiostat and the cell-generated voltages become equal. As previously confirmed, both measured parameters are directly related to one-to-one dependence of the (101) Anatase peak intensity. Comparing the I(V) characteristics, it becomes obvious, that the thicker films (225 nm) adsorbed more of the ruthenium dye and electrolytes than the thinner one (170 mm). The cells with no bias applied, or up to -50 V, were more efficient, for example the Fill Factor (FF) of 6-M2* reaches 0.62. The maximum current density per cell with equivalent thickness of 1000 nm should be 8.4 mA/cm² with conversion efficiency of $\eta = 2.73\%$. The latter assumption is based on a linear data extrapolation on the characteristics of the electrical cells, remembering that the cell transparency is not affected at thicknesses up to 1 μm.

Degradations of the cell electrical parameters are related with power dissipation across internal resistances, which was modelled as a parallel shunt resistance (R_{SH}) and series resistance (R_S). When R_{SH} is not infinite, the I(V) saturation region drops in such manner that I_{SC} could vanish further. These losses are due to poor electrical contact at electrodes and shortening when electrolyte becomes into contact with the electrodes resulting in charge leakage. The "permeability" of the used BL and its well-defined Anatase structure is important. The R_S increase slows-down the I_{SC} and in general reflects poor porosity as those cavities accommodate the dye and the electrolyte. The cavities should be interconnected, which is a mandatory condition. Here, again the purity of the Anatase phases maintain not only the desired porosity but also contribute to charge exchanges in the most effective way.

Table 4 provides data on the grain dimensions of the porous films together with the thicknesses of the films. The anatase microcrystals are oriented and grouped in specific grains. The bias refers only to the porosity of compact films deposited, whose structure and chemistry predetermine the nature of the porous TiO_2 film. The obtained results are coherent with the I(V) characteristics, and the larger grain sizes are associated with higher I_{SC} and V_{OC} parameters. The deduced grain size (Scherrer's equation) based on the reflections of planes (101) of the anatase tetragonal structure coincide with those shown in the histogram (Figure 3). As all reflecting plans constitute half of the microcrystals size, these values (D [nm], Table 4) should be doubled. Sample M6 with midsized grain of 86.5 nm draws our attentions. Not by chance, M6 cell has the highest FF (Table 3. and Figure 11) which indicates

Table 3. Summarized data based on the XRD patterns and I(V) cell characteristics for sample numbers 3 and 6.

Sample	Peak counts (101)	FWHM	V_{OC} [V]	R_S [Ω]	J_{SC} [mA/cm2]	FF
6	660	0.15	0.74	170	1.0094	0.615
3	730	0.17	0.66	312	1.063	0.45

Table 4. Grain size of porous TiO_2/BL deduced by (101) anatase plane reflections

Thickness [nm]	225 nm				175 nm			
Porous	M1	M2	M3	M4(A+R)	M5	M6	M7	M8
D [nm]	40	47.5	46.5	30	72.3	86.5	32	28.5
Bias [V]	0	-50	-100	-200	0	-50	-100	-200

perfect shunt resistance (lack of slope in the region above I_{SC}). This structure ensures semiconductor with optimal porosity, good interconnectivity, and charge throughput.

4. Conclusions

This work shows how and to what extent the structure of the compact BL deposited between the FTO electrode and the porous titanium dioxide film defines the nature of the latter and plays a decisive role on the photoelectrochemical parameters of DSSCs. The compact blocking layers and the porous TiO_2 thin films were deposited *in situ* by dual DC/HiPIMS, and the DSSCs were assembled and characterized. The crystalline structure, the morphology, and the chemical state of the BLs were investigated with respect to the negative substrate polarization applied during the film growth. The compact layer structure, managed mainly by the substrate polarization, defined the quality of the adjacent porous TiO_2 layers, which reflects on the characteristics and efficiency of the I(V) solar cells. The compact BLs exhibited exponential decay law of the surface energy as a function of the polarization, with decay constant at around 40 V. The XPS study of the compact layers found that the surface of the shake-up satellite of the doublet $Ti\ 2p_{3/2} - Ti\ 2p_{1/2}$ follow exponential decay law as well as the polarization rises. This shake-up satellite surface decrement means reduction of the Ti^{4+} states or its descending to lower homological states than the TiO_2. The two obtained decay constants were distinctly similar, which unambiguously connect both phenomena – the film surface energy and the Ti^{4+} oxidation state typical for the high quality Anatase structure. Any ion flux in the range of $1-1.4.10^{17}$ at/cm²/s lead to optimal crystalline structure with optimal surface energy. The latter is required and a sufficient condition for efficient cell formation by equal film chemistry, electrodes materials, and thicknesses. Figure 8 and 9 unprecedently show the one-to-one dependencies of I_{SC} and V_{OC} on the TiO_2 crystalline structure and phase composition. These inferences are largely applicable to the advanced photoelectrochemical and perovskite-based solar cells.

5. Acknowledgments

6. References

1. O'Regan B, Grätzel M. Synthesis and characterization of metal organic chemical vapour deposited copper titanium oxide (Cu-Ti-O) thin films from single solid source precursor. Nature. 1991;353:737.

2. Kao MC, Chen HZ, Young SL, Kung CY, Lin CC. The effects of the thickness of TiO2 films on the performance of dye-sensitized solar cells. Thin Solid Films. 2009;517(17):5096-9. http://dx.doi.org/10.1016/j.tsf.2009.03.102.

3. Hodes G. Photoelectrochemical cell measurements: getting the basics right. J Phys Chem Lett. 2012;3(9):1208-13. http://dx.doi.org/10.1021/jz300220b.

4. Mao X, Zhou R, Zhang S, Ding L, Wan L, Qin S, et al. High efficiency dye-sensitized solar cells constructed with composites of TiO_2 and the SnO_2 nanocrystals. Sci Rep. 2016;6(1):19390. http://dx.doi.org/10.1038/srep19390.

5. Lindgren T, Mwabora JM, Avendaño E, Jonsson J, Hoel A, Granqvist C-G, et al. Photoelectrochemical and optical properties of nitrogen doped titanium dioxide films prepared by reactive DC magnetron sputtering. J Phys Chem B. 2003;107(24):5709-16. http://dx.doi.org/10.1021/jp027345j.

6. Kim HJ, Jeon JD, Kim DY, Lee JJ, Kwak SY. Improved performance of dye-sensitized solar cells with compact TiO_2 blocking layer prepared using low-temperature reactive ICP-assisted DC magnetron sputtering. J Ind Eng Chem. 2012;18(5):1807-12. http://dx.doi.org/10.1016/j.jiec.2012.04.008.

7. Meng L, Li C. Blocking layer effect on dye-sensitized solar cells assembled with TiO_2 nanorods prepared by dc reactive magnetron sputtering. Nanosci Nanotechnol Lett. 2011;3(2):181-5. http://dx.doi.org/10.1166/nnl.2011.1143.

8. Braga A, Baratto C, Colombi P, Bontempi E, Salvinelli G, Drera G, et al. An ultrathin TiO2 blocking layer on Cd stannate as highly efficient front contact for dye-sensitized solar cells. Phys Chem Chem Phys. 2013;15(39):16812. http://dx.doi.org/10.1039/c3cp52250d.

9. Kment S, Krysova H, Hubicka Z, Kmentova H, Kavan L, Zboril R. Very thin thermally stable TiO_2 blocking layers with enhanced electron transfer for solar cells. Appl Mater Today. 2017;9:122-9. http://dx.doi.org/10.1016/j.apmt.2017.05.008.

10. Selopal GS, Milan R, Concina I, Sberveglieri G, Vomiero A. Effect of blocking layer to boost photoconversion efficiency in ZnO dye-sensitized solar cells. ACS Appl Mater Interfaces. 2014;6(14):11236-44. http://dx.doi.org/10.1021/am501360a.

11. Woo J-S, Jang G-E. A comparative study on the various blocking layers for performance improvement of dye-sensitized solar cells. Trans Electr Electron Mater. 2013;14(6):312-6. http://dx.doi.org/10.4313/TEEM.2013.14.6.312.

12. Sung Y-M. Deposition of TiO_2 Blocking layers of photovoltaic cell using RF Magnetron Sputtering technology. Energy Procedia. 2013;34:582-8. http://dx.doi.org/10.1016/j.egypro.2013.06.788.

13. Islam N, Yang M, Zhu K, Fan Z. Mesoporous scaffolds based on TiO_2 nanorods and nanoparticles for efficient hybrid perovskite solar cells. J Mater Chem A Mater Energy Sustain. 2015;3(48):24315-21. http://dx.doi.org/10.1039/C5TA06727H.

14. Yella A, Mathew S, Aghazada S, Comte P, Grätzel M, Nazeeruddin MK. Dye-sensitized solar cells using cobalt electrolytes: the influence of porosity and pore size to achievehigh-efficiency. J Mater Chem C Mater Opt Electron Devices. 2017;5(11):2833-43. http://dx.doi.org/10.1039/C6TC05640G.

15. Gamry Instruments [homepage on the Internet]. Warminster; 2020 [2020 May 18]. Available from: https://www.gamry.com/application-notes/physechem/dssc-dye-sensitized-solar-cells/

16. Wang JTW, Ball JM, Barea EM, Abate A, Alexander-Webber JA, Huang J, et al. Low-temperature processed electron collection layers of graphene/TiO2nanocomposites in thin film perovskite solar cells. Nano Lett. 2014;14(2):724-30. http://dx.doi.org/10.1021/nl403997a.

17. Greczynski G, Lu J, Johansson M, Jensen J, Petrov I, Greene JE, et al. Selection of metal ion irradiation for controlling Ti1−xAlxN alloy growth via hybrid HIPIMS/magnetron co-sputtering. Vacuum. 2012;86(8):1036-40. http://dx.doi.org/10.1016/j.vacuum.2011.10.027.

18. Straňák V. High power impulse magnetron sputtering [thesis]. Greifswald: University of South Bohemia; 2011.

19. Grigorov KG, Oliveira IC, Maciel HS, Massi M, Oliveira MS Jr, Amorim J, et al. Optical and morphological properties of N-doped TiO$_2$ thin films. Surf Sci. 2011;605(7-8):775-82. http://dx.doi.org/10.1016/j.susc.2011.01.017.

20. Nakamura R, Tanaka T, Nakato Y. Mechanism for visible light responses in anodic photocurrents at N-Doped TiO$_2$ film electrodes. J Phys Chem B. 2004;108(30):10617-20. http://dx.doi.org/10.1021/jp048112q.

21. Boschloo G, Hagfeldt A. Characteristics of the iodide/triiodide redox mediator in dye-sensitized solar cells. Acc Chem Res. 2009;42(11):1819-26. http://dx.doi.org/10.1021/ar900138m.

22. Solaronix SA [homepage on the Internet]. Switzerland; 2020 [2020 May 18]. Available from: https://www.solaronix.com/materials/products/iodolyte

23. Chang HC, Huang HH, Wu CY, Hsu RQ, Hsu CY. The photocatalytic activity and compact layer characteristics of TiO$_2$ films prepared using radio frequency magnetron sputtering. Int J Photoenergy. 2014;2014:786165.

24. Grigorov KG, Bouchier D, Grigorov GI, Vignes J-L, Langeron J-P. A simple estimate of deposited energy and concentration profiles in films produced by Ion-Assisted Physical Vapour Deposition. Appl Phys, A Mater Sci Process. 1994;58(6):619-22. .

25. Grigorov GI, Grigorov KG, Sporken R, Caudano R. Ion-induced densification of PVD films: a choice of the optimum density of ion bombardment. Appl Phys, A Mater Sci Process. 1996;63(4):1-6.

26. Netterfield RP, Martin PJ, Pacey CG, Sainty WG, McKenzie DR, Auchterlonie G. Ion-assisted deposition of mixed TiO$_2$-SiO$_2$ films. J Appl Phys. 1989;66(4):1805-9.